ELSEVIER

Contents lists available at ScienceDirect

Chemical Geology

journal homepage: www.elsevier.com/locate/chemgeo



Invited Research Article



A lower bound on the rheological evolution of magmatic liquids during the 2018 Kilauea eruption

A. Soldati a, c, *, B.F. Houghton b, D.B. Dingwell a

- a Department of Earth and Environmental Sciences, Ludwig-Maximilians-Universität, München, Germany
- ^b Department of Earth Sciences, University of Hawai'i at Mānoa, Honolulu, HI, USA
- ^c Department of Marine, Earth, and Atmospheric Sciences, North Carolina State University, Raleigh, NC, USA

ARTICLE INFO

Editor: Balz Kamber

Keywords: Viscosity Rheology Kilauea

ABSTRACT

During the four month-long 2018 Kilauea Lower East Rift Zone (LERZ) eruption, the bulk chemical compositions of magma ranged from basalt to andesite. This compositional variety was reflected in eruptive style, which ranged from Hawaiian fountaining to Strombolian explosions. Here, we quantified the evolution of the melt viscosity of the eruptive products through high-temperature laboratory experiments performed on a representative sample set that was collected in the field immediately after the eruptive series. This suite of 18 samples comprises all major eruptive phases (early phase I, late phase II, phase III, fissure 17). The results illustrate the significant rheological variability of the eruptive products, and appear to link to variations in eruption dynamics. We propose a new standard for the rheological study of a multi-episode effusive eruption, whereby precise, near-real-time viscosity results are obtained during ongoing eruptions will become a routine component of volcano monitoring during future eruptive events.

Plain language summary: During the 2018 eruption of Kilauea, emerging magma spanned a wider compositional range than ever previously observed during a single eruption. This compositional diversity was matched by a variety in eruptive styles, which ranged from more persistent fountaining to short-lived explosions. Immediately after the eruption ceased, we collected a representative suite of 18 samples in the field, which comprises all major eruptive phases (early phase I, late phase I, phase II, phase III, fissure 17). We measured the melt viscosity of such samples through high-temperature laboratory experiments. The results illustrate a significant variability in viscosity, which is linked to the highly variable eruption dynamics. Here we propose a new standard for the study of multi-episode effusive eruptions from a viscosity standpoint. We hope and expect that this methodology will become routine practice during future eruption.

1. Introduction

1.1. Melt viscosity

Viscosity, i.e., the internal friction providing resistance to the flow of fluids, is arguably the material property of magmas, relevant to their transport and eruption, that exhibits the highest magnitude of variability (Spera, 2000). The viscosity of silicate melts depends strongly on temperature (T) and chemical composition (X). A change of $100\,^{\circ}\text{C}$ can translate into a shift of orders of magnitude in viscosity for a fixed composition. Likewise, at a given temperature, a variation in chemical composition from basaltic to andesitic may result in a variation of orders of magnitude in viscosity.

The viscosity of a silicate melt is commonly expressed as a function of temperature by fitting the available data to a non-Arrhenian Vogel-Fulcher-Tammann (VFT) equation (e.g., Vogel, 1921; Fulcher, 1925; Tammann and Hesse, 1926) of the form:

$$\log \eta = A + B/(T - C) \tag{1}$$

where A represents the (fictive) viscosity at infinite temperature, B is an activation energy, and C has the units of temperature; T is temperature in K.

Although empirical viscosity models (e.g. Giordano et al., 2008) now exist for the calculation of silicate liquid viscosities as a function of both temperature and composition, the detailed and sometimes subtle variations in viscosity that can be expected for successive erupted products

E-mail address: a.soldati@ncsu.edu (A. Soldati).

^{*} Corresponding author.

of multistage eruptions remain best investigated via direct experiments.

Variations in the rheology of relatively fluid, low-viscosity magmas may also play a role in their degassing efficiency and thus in eruptive style (e.g. Namiki and Manga, 2008). A variety of explosive activities (Hawaiian to Strombolian) were indeed observed during the 2018 Kilauea Lower East Rift Zone eruption (Gansecki et al., 2019; Neal et al., 2019), providing a suitable opportunity to further test this hypothesis.

Additionally, accurate knowledge of magma viscosity and its variation *during* an ongoing eruption has potential value in cases where ongoing real-time estimates of lava properties and simulations of lava advance and emplacement are being conducted as components of emergency management (Le Losq et al., 2015, Harris et al., 2017, Villeneuve et al., 2008, Harris et al., 2019). As a basis for magma viscosity estimates, the liquid viscosity will always be a crucial source of information from which deviations due to crystallinity and or vesicularity may impact the bulk viscosity (Harris and Allen III, 2008; Mader et al., 2013). In this paper, we focus on the viscosity baseline provided by liquid viscosity measurements.

Hopefully, near real-time lab-based experimental rheology will soon be within our grasp. This study details how once samples are obtained, a fine temporal scale reconstruction of the progression of magma liquid viscosity can be performed, with the potential of better constraining ongoing eruption scenarios.

1.2. 2018 Kilauea LERZ eruption sequence

The 2018 Kilauea lower East Rift Zone (LERZ) eruption started on May 3rd 2018, and lasted until approximately August 4th 2018. Magma was erupted from 24 distinct fissures. 23 of them were aligned, while one fissure (F17) was offset *en échelon* to the north-east by about 200 m. Several fissures experienced more than one eruptive episode. Based on geochemical data, the eruption has been divided in three main phases from the main fissure system and a fourth associated with F17, hereafter summarized after Gansecki et al. (2019).

Early phase I saw the opening of F1 to F15, between May 3rd and May 9th. Mostly transient, impulsive explosive eruptions (Fig. 1) fed several short lava flows. Late phase I lasted from May 12th to May 18th, and was marked by the opening of F16, F18 to F20, and F22, with a down-rift migration. Activity was also characterized by more powerful explosive eruptions, generating more widely travelled lavas. Overall, Phase I emplaced only 0.2% of the erupted volume. During Phase II, spanning from May 17th to May 27th, F21 and F24 opened up and several other fissures continued to erupt or were reactivated. Longer lava flows were emplaced, still accounting for only 3–7% of the eruptive volume. Phase III occurred between May 28th and August 4th, and was entirely focused on F8, where sustained low fountaining built a 28-m-high cone and fed a large, high velocity, channelized lava flow which entered the ocean and accounted for 92–96% of the total eruptive

volume. F17 was active between May 13th and 25th, overlapping with parts of late phase 1 and phase 2, with both Strombolian and Hawaiian eruptions (Fig. 1) and the emplacement of a sluggish flow field, amounting to about 0.5% of the total eruption volume. By the end of the eruption, the lavas covered 35.5 $\rm km^2$ of land (USGS, 2018).

Further details on the eruptive sequence can also be found in Neal et al. (2019).

2. Methods

2.1. Sample selection and preparation

Samples of rapidly quenched pyroclasts ejected during all eruptive phases were collected during or after the eruption from nine eruptive fissures: F2, F3, F9, F10 (early Phase I); F19, F22 (late Phase I); F24 (Phase II); and and F8w (Phase III). Additionally, nine samples were collected along fissure 17, because of its wide range of erupted compositions. From west to east they are named F17-A, F17-B, F17-C, F17-D, F17-E, F17-F, F17-G, F17-H, and F17-I. Sample locations are reported in Supplementary material 1 and shown in Supplementary material. 1.

Each rock sample was crushed and melted into a $Pt_{80}Rh_{20}$ cylindrical crucible in air in a Nabertherm® box furnace at 1500 °C for at least 30 min.

2.2. Liquid viscosity measurements

Superliquidus melt viscosities of each sample were measured at thermal and thermodynamic equilibrium, in air, via concentric cylinder viscometry, using a Brookfield DVIII+ measuring head (full torque range: 0–0.7187 mNm) and a modified Deltech® box furnace. In concentric cylinder viscometry, a cylindrical spindle is immersed in a cylindrical crucible and rotated at constant speed. The torque exerted by the sample on the rotating spindle is proportional to the melt viscosity. The spindle used for these experiments is composed of $Pt_{80}Rh_{20}$ and is iron-saturated. It consists of an immersed section with a length of 33.2 mm, a diameter of 14.4 mm, and 45° conical top and bottom terminations, attached to a 2.4 mm diameter stem which widens to 3 mm above the immersion level. The measuring crucible, also made of $Pt_{80}Rh_{20}$ and iron-saturated, is 51 mm high with a diameter of 26.6 mm.

The crucible-spindle pair was calibrated against standard glass DGG 1 (Meerlender, 1975). Additionally, a temperature calibration, which spanned the entire experimental temperature range, was performed by immersing a Pt-sheathed Type S thermocouple in a standard DGG1 glass melt and comparing the measurements obtained from the immersed thermocouple with those from the continuously monitored control temperature thermocouple (Type B) with which the furnace is operated. The rotation-rate-based viscometer calibrations over the range of rotation rates used in the experiments were performed by comparing

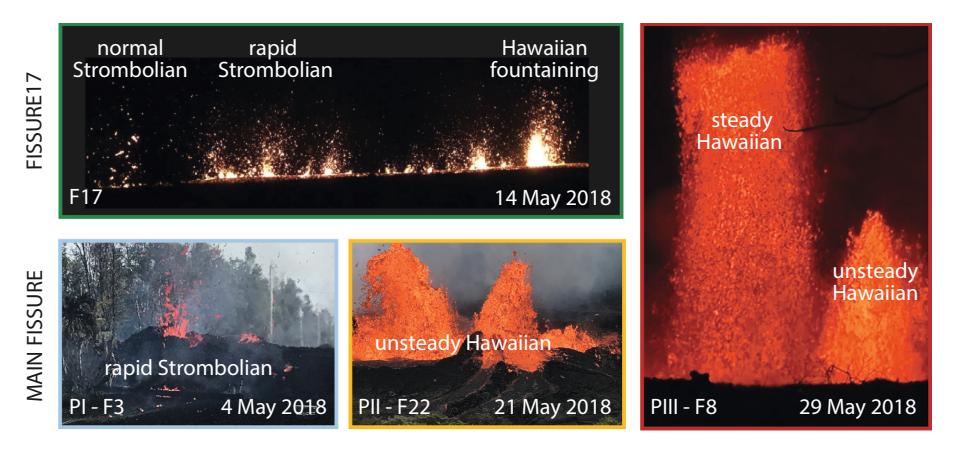


Fig. 1. Eruptive styles observed throughout the eruption.

measured torque readings with certified viscosity values from calibrated temperatures for the DGG1 standard melt. The precision of these viscosity determinations is $\pm 3\%$ (Dingwell, 1986).

The experimental protocol employed here started at superliquidus conditions (control temperature = 1500 $^{\circ}$ C), where the sample was held and constantly stirred for at least 3 h. This ensured the complete homogenization of the sample, and the dissolution of any oxides present, which is confirmedd by their absence in post-experimental analyses. Temperature was then reduced in 25 °C steps until the onset of crystallization. Crystallization was detectable due to a long-term increase in bulk viscosity at constant temperature and led to cessation of the measurements in this study. Finally, the samples were reheated to control temperatures of 1500 °C to re-occupy the initial conditions and thus check for any instrumental or sample drift - none was detected. Each temperature step involved a one-hour dwell to allow for thermal relaxation of the sample and furnace. The initial rotation speed at 1500 °C was 40 rotations per minute (RPM) for all samples, and was then automatically halved with falling temperature whenever the torque exceeded 100%, down to a minimum value of 0.1 RPM. All viscometry measurements were performed at LMU Munich, and the experimental protocol is also described in Chevrel et al. (2015).

2.3. Sample chemical characterization

The bulk chemical compositions of the post-experimental glasses were determined by electron probe micro-analyser (EPMA) performed with a Cameca SX100 instrument using 15 kV accelerating voltage and 10 nA beam current at LMU Munich. At least 10 spot analyses (spot size: $10~\mu m$) were performed for 10~s peak counting times (5 s background on

each side) and averaged for each sample. All totals lie with the range 98.01 to 101.20 wt%. The results were normalized to 100%.

Additionally, glass EMPA analyses were performed on the natural samples. The analytical conditions applied were the same as for the post-experimental glasses. These analyses were used for geothermometry.

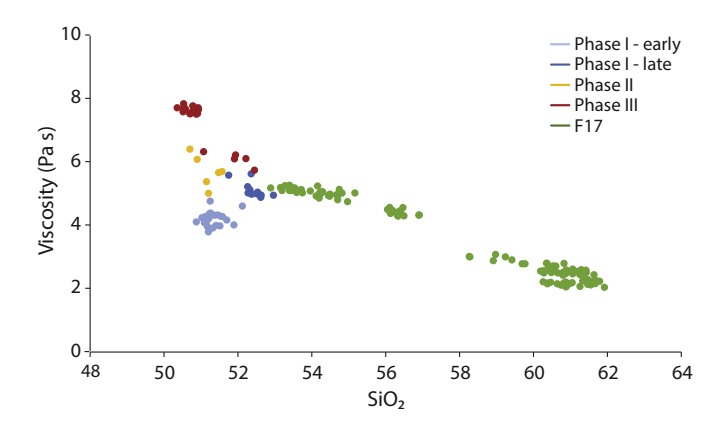


Fig. 2. SiO₂ vs MgO Harker diagram of the 2018 Kilauea LERZ eruptive products. EPMA analyses conducted on bulk remelted samples.

Table 1Normalized post-experimental glass bulk EMPA analyses.

Phase	Fissure	${ m SiO_2}$	TiO_2	Al_2O_3	FeO	MgO	MnO	Na_2O	K_2O	CaO	P_2O_5	Cr_2O_3	Total
Phase I -	F2	51.24	4.79	11.96	14.61	4.02	0.21	2.94	1.07	8.50	0.64	0.02	100.00
early		(0.30)	(0.08)	(0.11)	(0.15)	(0.11)	(0.03)	(0.17)	(0.03)	(0.09)	(0.02)	(0.02)	(98.50*)
	F3	51.34	4.52	12.56	13.89	4.25	0.22	3.09	1.01	8.51	0.60	0.01	100.00
		(0.21)	(0.07)	(0.11)	(0.15)	(0.08)	(0.03)	(0.09)	(0.06)	(0.07)	(0.04)	(0.02)	(98.35*)
	F9	51.36	4.77	12.27	14.09	4.32	0.21	3.07	0.98	8.37	0.56	0.01	100.00
		(0.49)	(0.05)	(0.28)	(0.46)	(0.43)	(0.03)	(0.27)	(0.08)	(0.22)	(0.05)	(0.01)	(98.95*)
	F10	51.40	4.37	12.80	13.58	4.28	0.19	3.16	0.97	8.70	0.55	0.00	100.00
		(0.15)	(0.07)	(0.17)	(0.11)	(0.05)	(0.02)	(0.08)	(0.01)	(0.06)	(0.02)	(0.00)	(98.74*)
Phase I -	F19	52.08	3.16	13.07	12.56	5.28	0.21	2.80	0.74	9.73	0.36	0.01	100.00
late		(0.32)	(0.06)	(0.03)	(0.15)	(0.25)	(0.03)	(0.09)	(0.04)	(0.07)	(0.02)	(0.01)	(98.29*)
	F22	52.48	3.33	12.98	12.56	5.03	0.19	2.94	0.79	9.32	0.38	0.01	100.00
		(0.21)	(0.06)	(0.09)	(0.17)	(0.22)	(0.03)	(0.04)	(0.04)	(0.12)	(0.03)	(0.01)	(98.41*)
Phase II	F24	51.13	2.89	13.76	12.12	5.68	0.20	2.77	0.45	10.68	0.30	0.02	100.00
		(0.33)	(0.14)	(0.23)	(0.77)	(0.50)	(0.01)	(0.16)	(0.09)	(0.42)	(0.04)	(0.02)	(99.55*)
Phase III	F8	50.67	2.59	13.39	11.38	7.64	0.17	2.46	0.45	10.93	0.26	0.06	100.00
		(0.18)	(0.06)	(0.12)	(0.15)	(0.10)	(0.04)	(0.04)	(0.03)	(0.09)	(0.04)	(0.04)	(99.33*)
	F8w	51.88	2.93	13.61	11.69	6.07	0.17	2.01	0.52	10.76	0.31	0.04	100.00
		(0.52)	(0.08)	(0.13)	(0.18)	(0.22)	(0.03)	(0.08)	(0.02)	(0.07)	(0.02)	(0.01)	(98.94*)
F17	F17 - A	60.74	1.74	14.15	9.34	2.11	0.17	4.04	1.69	5.47	0.53	0.01	100.00
		(0.27)	(0.08)	(0.13)	(0.27)	(0.05)	(0.03)	(0.09)	(0.06)	(0.15)	(0.06)	(0.03)	(99.10*)
	F17-B	61.53	1.74	13.71	9.26	2.16	0.20	3.74	1.75	5.32	0.55	0.03	100.00
		(0.22)	(0.10)	(0.16)	(0.28)	(0.08)	(0.06)	(0.10)	(0.10)	(0.15)	(0.07)	(0.03)	(99.45*)
	F17-C	59.75	2.25	13.43	9.74	2.80	0.16	3.77	1.60	6.04	0.43	0.02	100.00
		(0.87)	(0.25)	(0.11)	(0.45)	(0.14)	(0.07)	(0.18)	(0.07)	(0.22)	(0.08)	(0.03)	(99.69*)
	F17 - D	60.66	1.83	13.94	8.88	2.48	0.16	4.21	1.72	5.65	0.45	0.02	100.00
		(0.29)	(0.07)	(0.12)	(0.15)	(0.04)	(0.04)	(0.14)	(0.04)	(0.12)	(0.05)	(0.02)	(99.27*)
	F17 - E	61.16	1.76	13.93	8.78	2.49	0.16	3.93	1.69	5.67	0.42	0.02	100.00
		(0.22)	(0.08)	(0.12)	(0.12)	(0.06)	(0.05)	(0.09)	(0.06)	(0.10)	(0.03)	(0.02)	(99.20*)
	F17-F	56.35	2.49	13.46	10.22	4.38	0.15	3.45	1.16	8.01	0.32	0.03	100.00
		(0.27)	(0.09)	(0.16)	(0.20)	(0.10)	(0.05)	(0.11)	(0.07)	(0.19)	(0.06)	(0.03)	(99.86*)
	F17-G	54.51	2.81	13.37	11.05	4.95	0.17	3.01	0.97	8.74	0.40	0.02	100.00
		(0.34)	(0.09)	(0.22)	(0.21)	(0.13)	(0.06)	(0.12)	(0.08)	(0.20)	(0.07)	(0.03)	(99.50*)
	F17 - H	54.10	2.72	13.65	11.17	5.00	0.17	3.15	0.95	8.74	0.33	0.02	100.00
		(0.32)	(0.09)	(0.10)	(0.05)	(0.07)	(0.07)	(0.03)	(0.07)	(0.05)	(0.04)	(0.02)	(98.48*)
	F17 - I	53.33	2.91	13.60	11.65	5.12	0.18	3.02	0.91	8.86	0.40	0.02	100.00
		(0.21)	(0.08)	(0.14)	(0.09)	(0.07)	(0.03)	(0.07)	(0.04)	(0.14)	(0.03)	(0.03)	(98.64*)

All values provided are in wt%. Standard deviations are shown in parenthesis. The analyses are normalized to 100%. (*Original analytical totals are shown in parenthesis). Standards were as follows: albite (Si, Na), periclase (Mg), orthoclase (Al, K), apatite (P), wollanstonite (Ca), ilmenite (Fe), bustamite (Mn), chromite (Cr).

3. Results

3.1. Chemical composition

Post-experimental sample compositions are presented in Table 1 and plotted in Fig. 2. The samples from Phase I, II, and III are basaltic, whereas the samples from F17 are basaltic andesitic and andesitic. Samples from early Phase I have an average normalized SiO $_2$ content of 50.33 ± 0.53 wt%, which increases slightly to 50.91 ± 0.53 wt% during late Phase I. For Phase II samples the average SiO $_2$ content is 49.61 ± 0.18 wt%, and for Phase III it is 50.67 ± 0.18 wt%. MgO content (Fig. 2) increases markedly from early Phase I (4.88 \pm 0.09 wt%) to late Phase I (7.39 \pm 0.68 wt%), Phase II (7.68 \pm 0.06 wt%), and Phase III (7.67 \pm 0.10 wt%). Samples from F17 span a range of SiO $_2$ content, ranging from 53.38 \pm 0.25 wt% to 61.15 wt \pm 0.22 wt%. Their MgO content, which is negatively correlated with the SiO $_2$ content, is 2.11 \pm 0.03 wt% to 5.67 \pm 0.03 wt%.

3.2. Geothermometry

Eruptive temperatures were not measured during the eruption response. In order to infer eruptive temperatures we thus resorted to geothermometry. We applied the Helz and Thornber (1987) glass MgO geothermometer, which is specifically calibrated for Hawaiian lavas, to our natural sample suite. Resulting eruptive temperatures are 1095–1101 °C for early Phase I, 1115–1120 °C for late Phase I, 1128 °C for Phase II, 1168 °C for Phase III, and 1056–1117 °C for F17. The geothermometer's uncertainty is estimated to be ± 10 °C (Helz and Thornber, 1987).

3.3. Liquid viscosity

Liquid viscosity data are plotted in Fig. 3, and further reported in Supplementary material 2. Liquid viscosity at 1483 °C (the highest sample temperature at which a measurement is available for all samples)

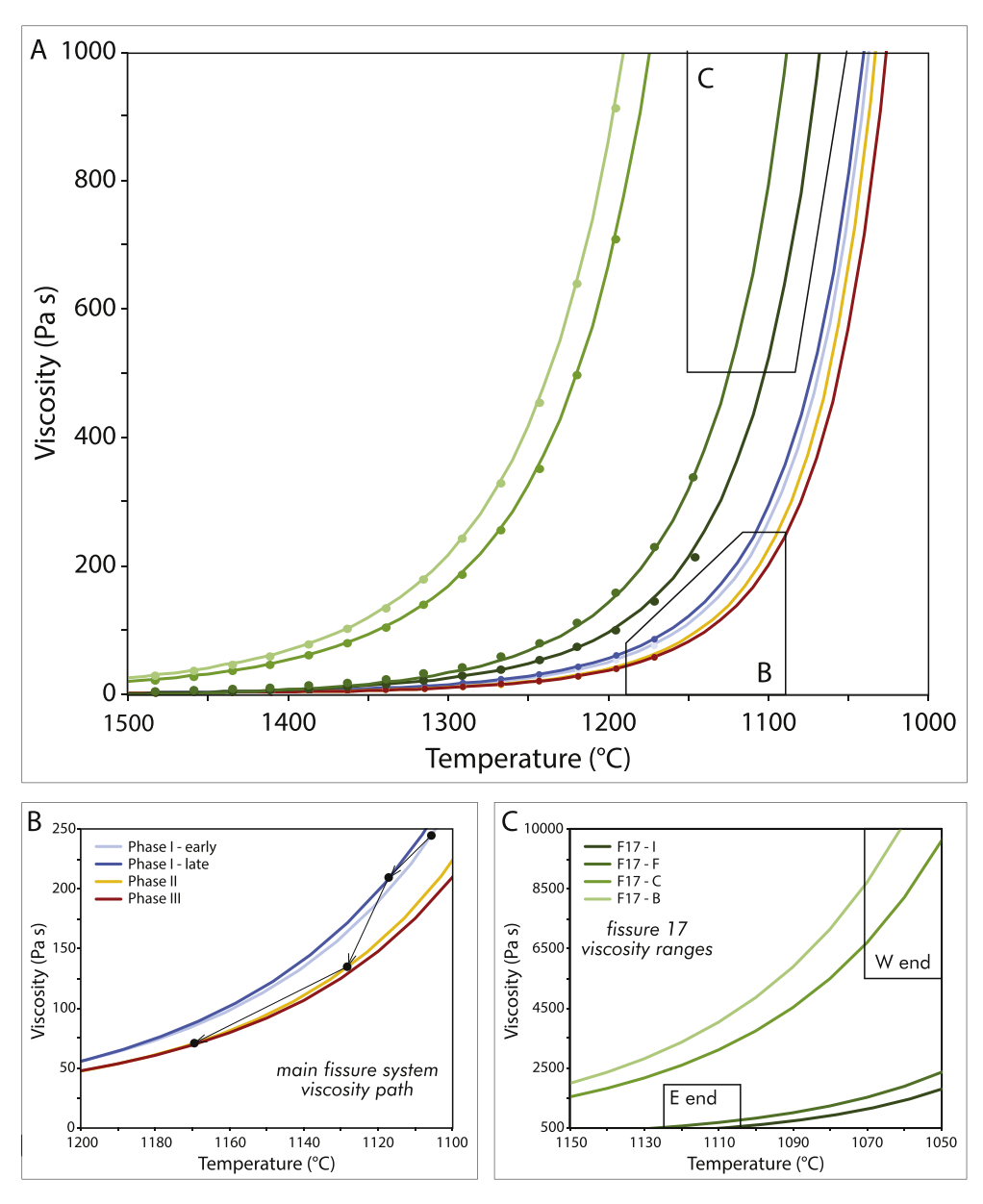


Fig. 3. 2018 Kilauea LERZ eruption liquid viscosity data (colored dots) and fits (colored curves). Black dots in panel B indicate viscosities corresponding to eruptive temperatures (as per geothermobarometry data); black arrows indicate the viscosity evolution of the main fissure system as the eruption progressed from early Phase I to Phase III. Black boxes in panel C indicate the temperature ranges for the F17 system, and the corresponding viscosity ranges.

A. Soldati et al. Chemical Geology 576 (2021) 120272

drops from 2.71 Pa s for Phase I samples to 2.59 Pa s for late Phase I samples to 1.89 Pa s for Phase III samples and 2.43 Pa s for Phase III samples. At the same temperature, F17 samples display higher viscosities, ranging from 4.85 Pa s for sample F17-I to 31.0 Pa s for sample F17-B. Liquid viscosity at 1172 °C (the lowest sample temperature at which a measurement is available for all samples) spans from an average of 74.6 Pa s for early Phase I samples through 80.9 Pa s for late Phase I samples to 57.2 Pa s for Phase II samples and 60.0 for Phase III samples. At the same temperature, F17 samples display higher viscosities, ranging from 145 Pa s for sample F17-I to 1330 Pa s for sample F17-B.

4. Discussion

The sample suite in this study spans the entire compositional range of the eruption, from the primitive basalt of Phase III to the andesite of western F17. In order to analyse the actual viscosity evolution of the aserupted 2018 Kilauea LERZ products, both compositional and temperature information is needed.

Silica content has a first-order effect on viscosity of silicate melts. The silica content variability is limited for the main fissure samples (50–53 wt%), but much wider for the fissure 17 samples (53–62 wt%). This is reflected in the higher and more scattered viscosity values of fissure 17 melts, with the western end being more silica-rich and thus more viscous than the eastern end. Magnesium content also affects melt viscosity, with higher magnesium contents leading to lower melt viscosities. Magnesium content increased throughout the eruption from 4.4 wt% in early Phase 1 to 6.9 wt% in Phase 3, whereas viscosity decreased. We note that magnesium content was lower on average in Fissure 17 samples, but their much higher silica content offset the effect of magnesium and still resulted in overall higher melt viscosities.

Viscosity measurements were obtained across a wide range of superliquidus temperatures, due to the strong dependence of viscosity on temperature (e.g. Giordano et al., 2008), we must constrain the emplacement thermal conditions in order to apply our experimental results to the 2018 eruption.

Whereas Gansecki et al. (2019) applied the Giordano et al. (2008) model to compositional analyses of matrix glasses in order to model the viscosity of the magma emitted during the various eruption stages here we measured the viscosities of bulk remelted samples, then fitted our data with the VFT equation (Vogel, 1921), and finally obtained the composition-specific viscosity at the emplacement temperature of the magma of each eruptive phase (Table 2). To date, the results presented in this study represent the most complete dataset on the viscosity of any multi-episode eruption. Our data clearly show how viscosity can change across three orders of magnitude at magmatic temperatures as extracted magma composition changes within the course of a single eruption. Fig. 4 shows that melt viscosity generally decreased as the eruption proceeded (230 to 258 Pa s in early Phase I, 180 to 224 Pa s in late Phase I, 119 Pa s in Phase II, 64 Pa s in Phase III), whereas F17 consistently emitted much higher and highly variable viscosity magma (366 to 10,800 Pa s). The ± 10 °C uncertainty in geothermometry (Helz and Thornber, 1987) yields a very uncertainty in viscosity of ± 0.1 log units over the temperature and composition range considered here.

It is important to notice that our measurements used remelted bulk samples as starting materials. The viscosity results obtained must therefore be considered as lower limits, as the erupted lava consists of a somewhat more evolved melt component containing crystals and bubbles. An additional factor to be considered is iron redox state, which is temperature-dependent, as oxidized melts are slightly more viscous than equivalent reduced melts (e.g. Dingwell and Virgo, 1988). We provide a detailed study of the crystallization dynamics and consequent viscosity evolution of these samples in a separate contribution (Soldati et al., 2021).

The effects of viscosity evolution throughout the eruption are reflected in the variety of observed eruptive styles (Fig. 4). Early Phase I displays the highest viscosity of the main fissure system magma. This

Table 2 Liquid viscosity VFT fit. Temperature is in $^{\circ}$ C, viscosity is in Pa s.

Phase	Vent	A	В	С	T	η
Phase I - early	F2	-3.28	4129.98	642.17	1095	256
	F3	-3.29	4164.04	641.83	1099	258
	F9	-3.37	4294.24	626.08	1101	235
	F10	-3.40	4362.74	615.96	1100	230
Phase I - late	F19	-3.30	3989.11	674.94	1120	180
	F22	-3.32	4098.00	665.31	1115	224
Phase II	F24	-3.15	3534.25	724.91	1128	119
Phase III	F8	-2.26	2386.61	854.19	1168	64
F17	F17-A	-3.69	6737.93	456.14	1056	10,700
	F17-B	-3.48	6265.88	496.30	1057	10,800
	F17-C	-3.60	6313.51	490.94	1070	6430
	F17-D	-3.55	6220.58	502.97	1064	8080
	F17-E	-3.57	6300.69	500.84	1064	9200
	F17-F	-2.76	3846.08	694.43	1102	776
	F17-G	-2.73	3590.18	715.38	1113	419
	F17-H	-2.69	3555.99	725.96	1115	479
	F17-I	-2.78	3609.56	714.65	1117	366

magma is thought to be residual magma stored for a long time in the shallow plumbing system (Gansecki et al., 2019). It erupted in rapid Strombolian explosions and very weak unsteady fountaining that fed viscous short-travelled mostly 'a'ā lavas. New hotter magma later replenished the feeding system for the remainder of the main fissure eruption. Little variability is observed in the eruptive activity of fissures of late Phase I to Phase II, (unsteady Hawaiian fountaining feeding lava flows) and reflects that the viscosity remained consistent. The eruption escalated and focused on a single point source vent in Phase III with steady (and unsteady) Hawaiian fountaining. The lowest viscosity magma produced is that emitted during Phase III, feeding the fastest and most travelled lava. The offset fissure 17 emitted unusually evolved magma. Its viscosity is much greater than that of the rest of the magma emitted during this eruption, and spans a wider range. Specifically, the western end of fissure 17 emitted more evolved, higher-viscosity andesitic magma, whereas the eastern part emplaced relatively less evolved, lower-viscosity basaltic andesite magma. The eruptive activity observed reflects this wide compositional and viscosity range: from normal Strombolian explosions at the western end, to rapid Strombolian activity in the center and Hawaiian fountaining at the easternmost vent.

These results demonstrate that variations on eruptive style can be linked to experimentally-based quantitatively estimated melt viscosities at a level of precision which will hopefully prove useful for future real-time monitoring of volcanic eruptive events.

5. Conclusions

The main findings of this work are as follows:

- The viscosity observed during the 2018 Kilauea LERZ eruption varies across three orders of magnitude, reflecting principally magma composition evolution.
- 2. The viscosity of magma emitted from the main fissure system decreased progressively as the eruption went on.
- The magma emitted at Fissure 17 displays a significantly higher viscosity than that of the main fissure system, and has a wider variability.
- 4. The eruptive activity spectrum observed during the eruption was strongly influenced by the viscosity evolution of the erupted magma: from Hawaiian fountaining for the main fissure system and the easternmost part of Fissure 17, to Strombolian for the westernmost part of Fissure 17.

Declaration of Competing Interest

The authors declare that they have no known competing financial

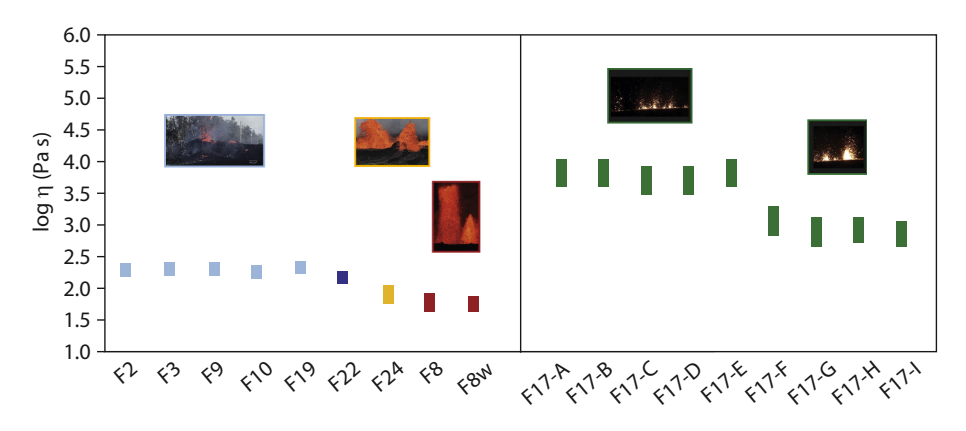


Fig. 4. 2018 Kilauea LERZ eruption bulk liquid viscosity evolution. Color coding consistent with previous figures according to eruptive phase. Inset photos from Fig. 1.

interests or personal relationships that could have appeared to influence the work reported in this paper.

Acknowledgements

We thank Dirk Müller and Corrado Cimarelli for technical assistance in the operation of the electron microprobe and scanning electron microscope facilities. Brett Walker and Caroline Tisdale collected many of the samples that we analyzed. We acknowledge the support and encouragement from staff of the Hawaiian Volcano Observatory throughout the field work. This research was funded by the Alexander von Humboldt Postdoctoral Fellowship to AS. BFH's contribution was funded by NSF EAR-1829188. DBD acknowledges the support of ERC-2018-ADG Grant 834225 (EAVESDROP).

Appendix A. Supplementary data

Supplementary data to this article can be found online at https://doi.org/10.1016/j.chemgeo.2021.120272.

References

Chevrel, M.O., Cimarelli, C., deBiasi, L., Hanson, J.B., Lavallée, Y., Arzilli, F., Dingwell, D.B., 2015. Viscosity measurements of crystallizing andesite from Tungurahua volcano (E cuador). Geochem. Geophys. Geosyst. 16 (3), 870–889.

Dingwell, D.B., 1986. Viscosity-temperature relationships in the system Na₂Si₂O₅-Na₄Al₂O₅. Geochim. Cosmochim. Acta 50 (6), 1261–1265. https://doi.org/10.1016/0016-7037(86)90409-6.

Dingwell, D.B., Virgo, D., 1988. Viscosities of melts in the Na2O · FeO · Fe2O3 · SiO2 system and factors controlling relative viscosities of fully polymerized silicate melts. Geochim. Cosmochim. Acta 52 (2), 395–403.

Fulcher, G.S., 1925. Analysis of recent measurements of the viscosityof glasses. J. Am. Ceram. Soc. 8, 339–355.

Gansecki, C., Lee, R.L., Shea, T., Lundblad, S.P., Hon, K., Parcheta, C., 2019. The tangled tale of Kīlauea's 2018 eruption as told by geochemical monitoring. Science 366 (6470). https://doi.org/10.1126/science.aaz0147.

Giordano, D., Russell, J.K., Dingwell, D.B., 2008. Viscosity of magmatic liquids: a model. Earth Planet. Sci. Lett. 271 (1-4), 123-134. https://doi.org/10.1016/j. epsl.2008.03.038. Harris, A.J., Allen III, J.S., 2008. One-, two-and three-phase viscosity treatments for basaltic lava flows. J. Geophys. Res. Solid Earth 113 (B9).

Harris, Andrew J.L., Nicolas, Villeneuve, Di Muro, A., Ferrazzini, Valerie, Peltier, Aline, Coppola, Diego, Favalli, Massimiliano, et al., 2017. Effusive crises at Piton de la Fournaise 2014–2015: a review of a multi-national response model. J. Appl. Volcanol. 6 (1), 1–29.

Harris, A.J., Chevrel, M.O., Coppola, D., Ramsey, M.S., Hrysiewicz, A., Thivet, S., Gurioli, L., 2019. Validation of an integrated satellite-data-driven response to an effusive crisis: the April–May 2018 eruption of Piton de la Fournaise. Ann. Geophys. 62 (2), 230.

Helz, R.T., Thornber, C.R., 1987. Geothermometry of Kilauea Iki lava lake, Hawaii. Bull. Volcanol. 49 (5), 651–668. https://doi.org/10.1007/BF01080357.

Le Losq, C., Neuville, D.R., Moretti, R., Kyle, P.R., Oppenheimer, C., 2015. Rheology of phonolitic magmas—the case of the Erebus lava lake. Earth Planet. Sci. Lett. 411, 53–61.

Mader, H.M., Llewellin, E.W., Mueller, S.P., 2013. The rheology of two-phase magmas: a review and analysis. J. Volcanol. Geotherm. Res. 257, 135–158.

Meerlender, G., 1975. First standard glass from the Deutsche Glastechnische Gesellschaft and implementation of the viscosity scale at high temperatures. Rheol. Acta 14 (3), 279–290. https://doi.org/10.1007/BF01515966.

Namiki, A., Manga, M., 2008. Transition between fragmentation and permeable outgassing of low viscosity magmas. J. Volcanol. Geotherm. Res. 169 (1–2), 48–60. https://doi.org/10.1016/j.jvolgeores.2007.07.020.

Neal, C.A., Brantley, S.R., Antolik, L., Babb, J.L., Burgess, M., Calles, K., Damby, D., 2019. The 2018 rift eruption and summit collapse of Kīlauea Volcano. Science 363 (6425), 367–374.

Soldati, A., Houghton, B.F., Dingwell, D.B., 2021. The effect of bubbles on the rheology of basaltic lava flows: Insights from large-scale two-phase experiments. Earth Planet. Sci. Lett. 548, 116504.

Spera, W., 2000. Physical properties of Magma. In: Sigurdsson, Haraldur, Houghton, Bruce, Rymer, Hazel, Stix, John, McNutt, Steve (Eds.), Encyclopedia of Volcanoes. Academic Press, p. 1417.

Tammann, G., Hesse, W., 1926. Die Abhängigkeit der Viskosität von der Temperatur bei unterkühlten Flüssigkeiten. Z. Anorg. Allg. Chem. 156, 245–257.

U.S. Geological Survey Hawaiian Volcano Observatory, 2018. Preliminary Analysis of the Ongoing Lower East Rift Zone (LERZ) Eruption of Kilauea Volcano: Fissure 8 Prognosis and Ongoing Hazards (Cooperator Report to Hawaii County Civil Defense, 15 July 2018). https://volcanoes.usgs.gov/vsc/file_mngr/file-185/USGS%20Pre liminary%20Analysis_LERZ_7-15-18_v1.1.pdf.

Villeneuve, N., Neuville, D.R., Boivin, P., Bachèlery, P., Richet, P., 2008. Magma crystallization and viscosity: a study of molten basalts from the Piton de la Fournaise volcano (La Réunion island). Chem. Geol. 256 (3–4), 242–251.

Vogel, H., 1921. Temperaturabhängigkeitsgesetz der Viskosität von Flüssigkeiten. Phys. Z. 22, 645–646.